Available online at www.sciencedirect.com
ScienceDirect
Journal of Power Sources 161 (2006) 1469–1478
JOURNAL OF POWER SOURCES
www.elsevier.com/locate/jpowsour

Catalytic microcombustors with integrated thermoelectric elements for portable power production

J.A. Federici [a], D.G. Norton [a], T. Brüggemann [a], K.W. Voit [a], E.D. Wetzel [b], D.G. Vlachos [a,*]

[a] *Department of Chemical Engineering, Center for Catalytic Science and Technology, and Center for Composite Materials University of Delaware, Newark, DE 19716, United States*
[b] *Army Research Laboratory Aberdeen Proving Ground, MD 21005, United States*

Received 8 April 2006; received in revised form 19 May 2006; accepted 6 June 2006
Available online 31 July 2006

Abstract

In this study, catalytic microcombustors are integrated with thermoelectrics to produce electricity. The devices are found to be robust, easy to start up, and able to support complete combustion over a range of fuels (e.g., C_3H_8/air and H_2/air systems) at different flowrates. Various materials of construction for the microcombustors are investigated in order to yield good temperature uniformity, which is shown to increase electrical power output and efficiency. Electrical power generation from catalytic microcombustion with a thermal efficiency up to ∼0.8% is measured. Parameters affecting energy efficiency are also discussed.

Keywords: Microburners; Thermoelectrics; Power generation; Heat transfer; Temperature uniformity; Stability; Extinction; Hydrogen; Propane

1. Introduction

1.1. Compact devices for generation of power

In recent decades, there has been a dramatic increase in the number of consumer, industrial, and military applications utilizing portable electronic equipment, such as laptops, cellular telephones, and personal data assistants. All of these devices require a portable power source, which, most commonly, is provided by batteries. For many of these applications, however, the relatively low energy density of traditional batteries imposes burdensome weight and power limitations on system design. In addition, most of these battery chemistries rely on materials that are difficult to recycle and environmentally damaging to dispose of. Furthermore, the highest energy density batteries are often non-rechargeable. These single-use batteries present especially challenging economic, logistical, and environmental burdens for in-field military applications where there is limited infrastructure for battery supply and disposal.

Power generation utilizing hydrocarbons offers a promising alternative to traditional batteries. The energy density of hydrocarbons is significantly higher than that of batteries (approximately 40 MJ kg^{-1} versus 0.5 MJ kg^{-1} for lithium-ion battery chemistries) [1]. A hydrocarbon-based device with an overall efficiency of approximately 1% or greater can therefore lead to advancements in battery technology (under conditions where the fuel makes most of system's mass). Furthermore, hydrocarbon-based power systems can be quickly and repeatedly "recharged" simply by physical addition of more fuel.

Proton exchange membrane (PEM)-based fuel cells convert hydrogen directly into electricity. However, systems utilizing compressed H_2 produce low system-level energy density because of the high strength tanks required to store the gas at high pressures, and prevention of explosions is a concern. Direct methanol fuel cells (DMFCs) suffer from crossover of methanol from the anode to the cathode, which depresses the cell voltage and results in fuel loss [2]. System energy density is also reduced, since most DMFC devices require significant aqueous dilution of the methanol fuel. Solid oxide fuel cells are also being explored for the same objective [3].

Recent efforts have attempted to utilize combustion of hydrocarbons in miniature devices to directly produce heat or power

* Corresponding author. Tel.: +1 302 831 2830; fax: +1 302 831 1048.
E-mail address: vlachos@udel.edu (D.G. Vlachos).

0378-7753/$ – see front matter © 2006 Elsevier B.V. All rights reserved.
doi:10.1016/j.jpowsour.2006.06.042

[1,4–11]. These devices typically utilize conventional homogeneous (gas-phase) combustion, the same processes by which macroscopic flames produce heat. Homogeneous combustion generally results in very high operating temperatures (>1500 °C) [12,13], which is advantageous for some applications such as ammonia decomposition for hydrogen production [14,15]. However, these high temperatures also greatly limit material selection, require extensive combustor insulation, and lead to NO_x production. Thermal management is critical for device compatibility with electronics, packaging, and personnel, and can have additional implications for thermal signature in military systems. Furthermore, some of these microcombustion devices consist of complicated miniature parts, which are difficult and expensive to fabricate, and so far have exhibited efficiencies well below 1% [10].

An alternative to homogeneous microcombustion is to combust the fuel catalytically, without the production of a flame. When implemented in miniature devices, catalytic microcombustion has the potential to fully utilize the high energy densities of hydrocarbon fuels, but at much lower operating temperatures. Catalytic systems are also typically easier to start (possibly self-igniting as detailed in [8,9]) and self-sustained at leaner fuel/air ratios. Additionally, catalytic systems can be designed with very simple geometries and no moving parts, which dramatically reduces cost and simplifies miniaturization.

In this paper, we study integrated catalytic microcombustors with thermoelectric devices for the production of electrical power. The effect of fuel type and flow rate are investigated, as well as the importance of thermal management. Integration with external devices, such as a cooling fan and electronic device loads, are also explored. Finally, a discussion of the system-level chemical-to-electrical conversion efficiency is presented.

1.2. Design considerations for integrated microcombustor-thermoelectric devices

A thermoelectric device operates according to the Seebeck effect, where two materials with different Seebeck coefficients, when supporting a thermal gradient, as shown in Fig. 1, produce an electrical potential

$$V = \int_{T_1}^{T_2} (S_B(T) - S_A(T))\mathrm{d}T. \tag{1}$$

Here S_A and S_B are the Seebeck coefficients of materials A and B, respectively, T is the temperature, and V is the thermoelectric voltage. The dependence of S_A and S_B on temperature is often weak and can be neglected for simple calculations, giving

$$V = (S_B - S_A)(T_2 - T_1) = \Delta S \Delta T. \tag{2}$$

A thermoelectric device typically exhibits an internal resistance R_{int}. When coupled in series with a resistive device load R_{load}, the total generated current I is given by Ohm's law

$$I = \frac{V}{R_{int} + R_{load}}; \tag{3}$$

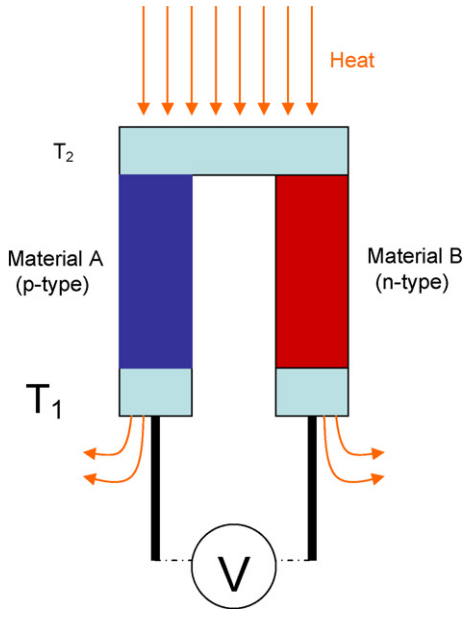

Fig. 1. Idealized schematic of a thermoelectric device.

therefore, the power P_{load} generated on the load is given by

$$P_{load} = R_{load}\left(\frac{\Delta S \Delta T}{R_{int} + R_{load}}\right)^2. \tag{4}$$

Electrical power can be generated from thermoelectrics by providing a source of heat to one face of the thermoelectric, and removing heat from the other face of the thermoelectric. Because the obtainable power from a thermoelectric device is proportional to the temperature differential squared (Eq. (4)), a successful power-generating device should be engineered to maximize the difference in temperatures between these two faces. However, thermoelectric devices usually have practical upper temperatures on the order of 200–300 °C. These limits are partly defined by melting and degradation temperatures for materials in the device or its packaging. The other limiting effect is the migration of dopants in the semiconductor components of the device.

Within these design requirements, the optimal power output can be achieved when the hot side temperature across the thermoelectric is uniform at the maximum allowable temperature, and the cold side temperature is uniform at the lowest practical temperature. To demonstrate this effect, we can use Eq. (4) to estimate the power output for a thermoelectric device subject to different hot side temperature profiles, assuming a peak temperature limit of 230 °C and a uniform cold side temperature of 30 °C for all cases. The thermoelectric device in these calculations is assumed to have 104 thermocouples with an average ΔS of 0.277 mV K^{-1} per thermocouple, and the experimentally measured resistances in our lab of $R_{int} = 5.3\ \Omega$ and $R_{load} = 5.3\ \Omega$ (these conditions are comparable to the devices discussed in this paper). Fig. 2 shows the predicted power output for a uniform hot side temperature profile, a linear decrease in temperature, and a profile with a peak temperature slightly downstream of the inlet. The uniform temperature profile shows the highest predicted power at 1.56 W. The profile with a peak temperature slightly downstream, which is similar to the temperature pro-

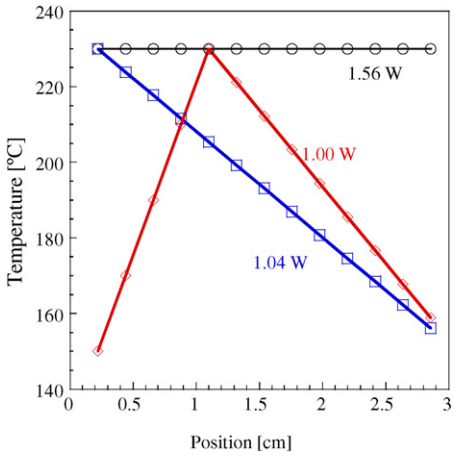

Fig. 2. Predicted thermoelectric generated power for different temperature profiles, represented by points, with maximum temperatures of 230 °C. The uniform temperature profile is predicted to produce more power than the non-uniform profiles. The cold side temperature is fixed at 30 °C.

file of propane/air combustion in our earlier combustors [8,9], shows significantly lower predicted power of P_{load} = 1.00 W. The profile with the peak temperature at the inlet and a decrease in temperature downstream, which is similar to the temperature profiles of the hydrogen/air combustion in our earlier work, shows a predicted power of P_{load} = 1.04 W. These differences in power outputs would further increase if larger spatial temperature gradients were assumed.

These simple calculations demonstrate that achieving temperature uniformity should be an important design goal for coupled microcombustor-thermoelectric devices. In our previous work [8,9], microcombustors made with ceramic-based housings were found to exhibit high maximum temperatures and thermal non-uniformity of several hundred degrees over a few centimeters. These features make these microcombustors unsuitable for integration with thermoelectrics. The problem of temperature non-uniformity in microchemical devices has also been raised several times in the literature [16,17]. Given these limitations of ceramic-based microburners, we have more recently fabricated a new generation of catalytic microburners utilizing metal combustor walls with integrated "thermal spreaders" for enhanced thermal uniformity [18]. The integration of these new microcombustors with thermoelectrics is discussed below.

2. Experimental

2.1. Device design and construction

The integrated system in this work consists of several parts: a catalytic microchannel combustor, thermal spreaders, a thermoelectric device, and a heat sink. A schematic of these parts is shown in Fig. 3a, a top view of the microcombustor is depicted in Fig. 3b, and a cross-sectional view of the microcombustor is displayed in Fig. 3c. The microcombustor fabrication has been detailed in [18]. Briefly, it consists of two rectangular sheets of 0.79 mm thick 316-alloy stainless steel, with a bolt pattern around the exterior. A thin (500 μm) gasket separates the two

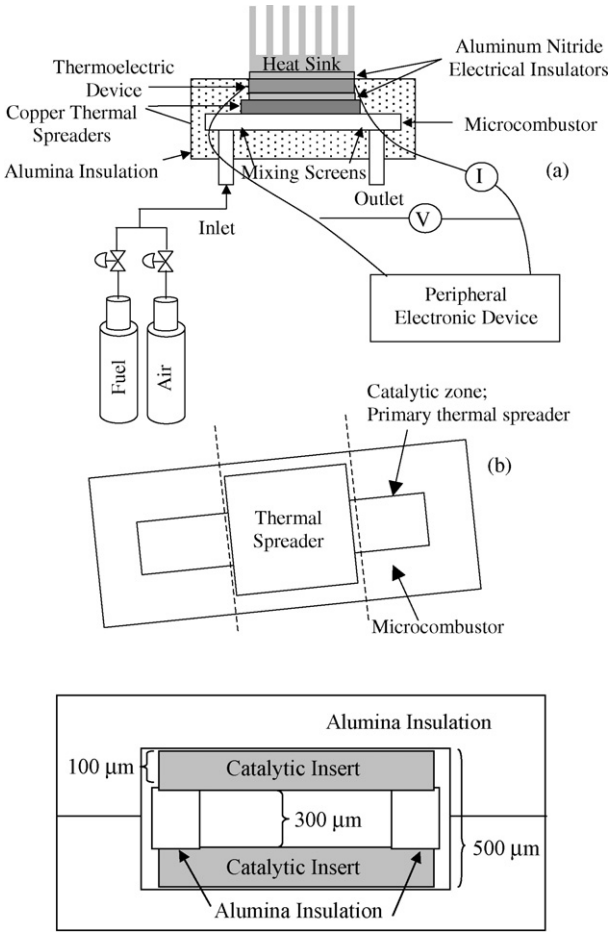

Fig. 3. (a) Schematic of the microcombustor/thermoelectric device, (b) schematic of top view of microcombustor and (c) cross-sectional view of microcombustor.

sheets to form a rectangular microchannel approximately 6 cm long by 1 cm wide. Stainless steel inlet and outlet tubes are welded to one of the exterior sheets. Fine metal screens are spot welded near the inlet and outlet of the channel in order to induce uniform flow over the microchannel. This reduces the effect of "jetting" that was witnessed in earlier work [9]. Platinum is deposited on thin (100 μm) alumina inserts, which are separated in the combustion chamber by 1-mm-wide alumina shims to create a total channel height of the catalytic section that is 300 μm, giving a reactor volume of 142 μL.

The catalytic inserts are formed by completely anodizing 75-μm-thick aluminum foil to create a large surface area alumina substrate. Fig. 4 shows the porous structure of the surface of the anodized alumina, which achieves a final thickness of approximately 100 μm because of the bulk expansion caused by anodization. Anodization creates a semi-ordered structure of pores, with approximately 2×10^{14} pores m^{-2} of support with diameters on the order of 50 nm.

Approximately 1500 m^2 of surface area is exposed for every geometric m^2 of alumina, resulting in approximately 14 m^2 per gram of alumina. Pt catalyst was deposited on the alumina substrates as detailed in [18]. Dark field high angle annular transmission electron micrographs were taken using a Jeol 2010F

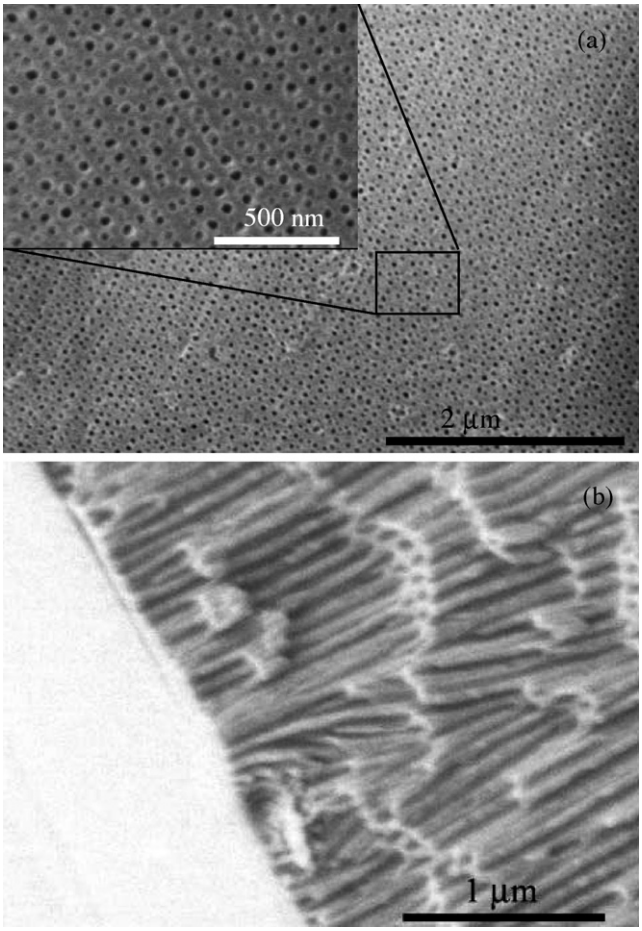

Fig. 4. SEM micrographs of (a) the top of the alumina insert surface and (b) the cross section of the insert. The pores have an average diameter of approximately 50 nm and travel the thickness of the insert.

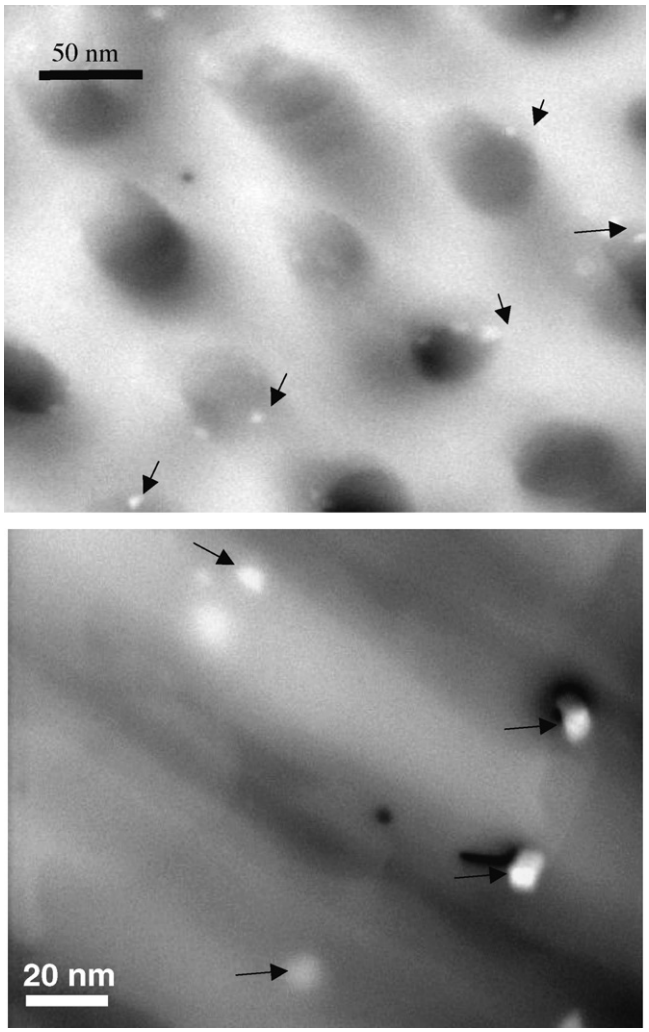

Fig. 5. TEM micrograph indicating (arrows) Pt nanoparticles on the top of the anodic alumina substrate (top) and inside the pores shown (bottom: alumina in gray). The average diameter of these particles is ∼8 nm.

TEM, and Pt nanoparticles were observed on both the surface and inside the alumina pores of the catalytic inserts, as shown in Fig. 5. The sample seen in this micrograph was calcined for 3 h at 500 °C, ground into a powder, and placed on a lacy carbon grid for imaging. Elemental mapping using EDAX software confirms that these nanoparticles are platinum.

The thick ceramic walls of our previous devices have been replaced in this work by metal components with integrated insulation layers, resulting in a more compact and rugged combustor. These insulating layers are blocks of fibrous alumina with a thickness of ∼6.4 mm. As detailed in [18], thermal spreaders of varying thermal resistance (conductivity and thickness) can be added to the combustor to decrease spatial thermal gradients. For our coupled microcombustor-thermoelectric device, two types of thermal spreaders are used. The "primary" thermal spreaders are 3.2 mm thick with the same 1 cm × 6 cm footprint as the catalytic section of the microchannel. The purpose of these primary thermal spreaders is to increase axial thermal uniformity along the microcombustor. For most experiments, the primary thermal spreaders are composed of copper, although a few experiments are performed using 316-alloy stainless steel (SS). The primary thermal spreaders are affixed to the exterior of the reactor using colloidal silver paste, obtained from Structure Probe, Inc. to ensure good thermal contact with the microcombustor walls. Square, 3.2 mm thick, 3.0 cm × 3.0 cm "secondary" thermal spreaders are placed on top of the primary thermal spreaders to transport heat uniformly over the full footprint of the thermoelectric device (see Fig. 3b). These secondary thermal spreaders are made of copper unless otherwise stated.

The thermoelectric modules used were Model HZ-2 from Hi-Z Technology, Inc. (San Diego, CA). The devices are approximately 2.9 cm wide × 2.9 cm long × 0.5 cm thick, and weigh 13.5 g. Two pieces of 1 mm thick aluminum nitride electrical insulating wafers are placed between the secondary thermal spreader and the thermoelectric device to prevent electrical shorting between thermoelectric elements. To ensure good thermal contact, thermal grease obtained from Hi-Z Technologies is placed between the primary and secondary thermal spreaders, electrical insulating wafers, and thermoelectric module. A finned copper heat sink, CoolWave CPU Cooler from Spire, is placed on top of the thermoelectric module to enhance convective cooling efficiency. To further ensure thermal contact, the entire microcombustor/thermal spreader/thermoelectric/heat sink stack was

placed under compressive force using a conventional C-clamp. The effect of compressive force is elaborated in Appendix A.

2.2. Combustor operation and measurement

To quantify power generation, the thermoelectric module was connected in series with a potentiometer to emulate the operation of a portable electronic device. A multimeter was used to measure load voltage and current as a function of load resistance by varying the resistance of the potentiometer. These voltage and current values were then used along with the internal resistance of the experimental setup to calculate a generated power value. In most cases, cooling was provided by natural convection, with slight forced convection provided by the updraft of the fume-hood in which the device was placed. For some experiments an external cooling fan, from Intel (part # 120115P), was placed on top of the heat sink to enhance convective cooling.

To determine temperatures throughout the system, thermocouples were installed above and below the thermoelectric module as well as directly above the reactor outlet. By placing a thermocouple directly above the reactor exit, the approximate temperature of the exiting gas can be measured for efficiency calculations. The hot side thermocouple was placed on the secondary, square thermal spreader, whereas the cold side thermocouple was placed at the approximate center of the heat sink. In addition, infrared (IR) imaging was used to interrogate spatial temperature profiles for both the un-insulated microcombustor and the integrated device in operation. A ThermoAlert N IR camera was used and calibrated using ThermoCAM Researcher 2000 software by measuring four points with thermocouples to set the emissivity of the entire system. Most imaged surfaces were coated with Aerodag G carbon paint from Acheson to ensure high emissivity.

Experiments are performed using H_2/air and C_3H_8/air fuel systems. The feed flow and composition are controlled using mass flow controllers from MKS Instruments. For all experiments, fuel/air mixtures are stoichiometric and the total flow rate is fixed at 1.4 standard liters per minute (SLPM), unless otherwise noted. Additional experiments with fuel-lean mixtures were also carried out (data not shown) and qualitatively similar results were obtained. The exhaust gases are sampled with a gas-sampling valve, and the composition is monitored with a HP Series 6890 gas chromatograph, using both a thermal conductivity detector and a flame ionization detector.

3. Results

3.1. Effect of thermal spreaders on temperature uniformity

It is evident from Fig. 2 that thermal uniformity is important for optimal thermoelectric performance. In order to evaluate the temperature uniformity of the microcombustor, thermal imaging was first performed for a microcombustor with primary and secondary thermal spreaders, but without insulating wafers, a thermoelectric module, or a heat sink. Fig. 6a shows an IR image of the top view of this setup, during H_2/air combustion at steady state. Fig. 6b shows the corresponding axial thermal profile along

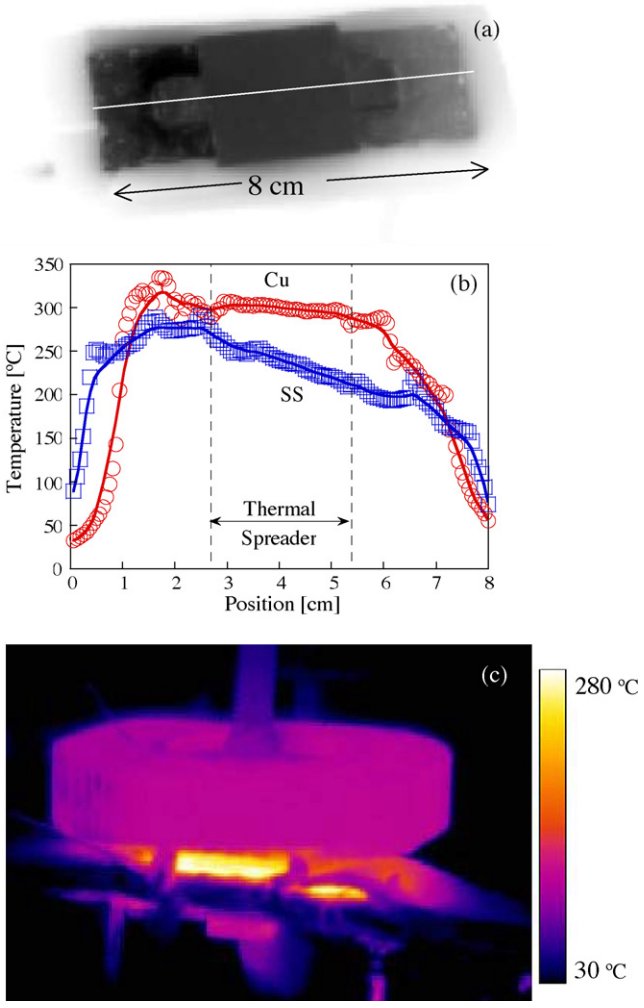

Fig. 6. (a) IR image of the top portion of the microcombustor with copper thermal spreaders, (b) corresponding temperature profile along the white line shown in panel a, using copper in both thermal spreaders (corresponding to panel a) and stainless steel (SS) in both thermal spreaders. The lines connect the points, (c) IR image of an integrated system. The operating conditions were a stoichiometric mixture of H_2/air at a total flow rate of 1.4 SLPM.

the center of the device. The temperature along the length of the secondary thermal spreader is uniform, with an average temperature of $299 \pm 8\,^{\circ}C$ in this region. Although the absence of a thermoelectric module and heat sink undoubtedly alters the overall thermal behavior of the system, these results indicate that the thermal spreaders are effective at providing a uniform heat source to the thermoelectric module.

Fig. 6b also show axial thermal profile for the case of a stainless steel primary thermal and secondary thermal spreader, measured using the same setup described above. The thermal profile for the stainless steel thermal spreader is significantly less uniform than that of the copper thermal spreader. This result is consistent with the results of Norton et al. [8], which showed that thermal inserts with higher thermal conductivity improve thermal uniformity.

Fig. 6c shows an IR image of the integrated (microcombustor and thermoelectric) device in operation during H_2/air combustion, using copper thermal spreaders. Fibrous alumina

enclosed all microcombustor and thermal spreader surfaces, with the exception of the sides of the secondary thermal spreader. The image shows that the temperature along the edge of the secondary thermal insert is very uniform. This result supports the supposition from Fig. 6a that the hot side of the thermoelectric module is probably fairly uniform in temperature.

However, Fig. 6c also shows that the heat sink temperature is ∼100 °C, indicating that heat removal from the thermoelectric is not fully efficient. The implications of this result for the efficiency of the device are discussed below.

3.2. Effects of fuel and flow rate on power generation

There are a number of important differences between H_2/air and C_3H_8/air microcombustion. As shown in previous work [8], H_2/air mixtures were found to be self-igniting. In contrast, C_3H_8/air mixtures were not self-igniting. Therefore, hydrogen assisted ignition [8] was utilized for propane combustion experiments, where a hydrogen/air mixture flows initially to ignite the system and hydrogen is then gradually replaced by propane.

Under stoichiometric conditions and a flow rate of 1.4 SLPM, hydrogen combustion in our device produces temperatures that are near the upper temperature limits of our thermoelectric modules, ∼300 °C. To avoid damage to the thermoelectric module, flow rates were decreased to 0.9 SLPM and below, which limits the upper temperature of the microcombustor to 226 °C. Note that these operating temperatures are significantly lower than the combustion temperatures reported in [8] under similar flow rates and compositions, due to the differences in thermal boundary conditions. In [8], the system was fully insulated, whereas in the present device the thermoelectric module and heat sink are integrated to extract heat from the microcombustor.

The differences in heat of combustion (2028 kJ mol^{-1} for propane as compared to 242 kJ mol^{-1} for hydrogen) [19] and in molar flow rates of the two fuels result in significantly higher operating temperatures, ∼500 °C, for propane/air combustion. The operating temperature of the device could be decreased somewhat by using lower flow rates and leaner mixtures, but the range of these adjustments is greatly limited by the relatively narrow window of operating conditions for self-sustained combustion for propane/air systems. For our particular device, we were unable to maintain self-sustained propane combustion at temperatures of 300 °C or below (something easy to obtain with hydrogen). Therefore, we instead replaced the single secondary thermal spreader with a 6.4 mm thick layer of fibrous alumina insulation sandwiched between two copper secondary thermal spreaders. This additional insulation allows the microcombustor to maintain higher temperatures, while limiting the thermoelectric module temperature to 250 °C or below. This approach clearly decreases the overall system efficiency, by allowing more energy to leave the system as enthalpy in the exhaust gases. However, it is sufficient to allow for demonstration of power production from propane using our existing device. Further discussion on improvements in thermal management will be addressed later in this manuscript.

The power generated using stoichiometric C_3H_8/air and H_2/air mixtures under different resistive loads for various flow rates are shown in Fig. 7a and b, respectively. The parabolic dependence of power generation on voltage reflects that power is maximized when the internal and load resistances are equal, which can be shown by calculating the maximum of Eq. (4). The results also show that power increases with flow rate. Increasing flow rate results in more fuel being heterogeneously combusted, which releases additional thermal energy and results in a higher hot side temperature (see Fig. 7c). Although the cold side temperature also increases slightly with flow rate, the increase in hot side temperature is more, resulting in a net temperature differential and power generation increase with flow rate. These differences are rationalized below.

In passing, we should mention that the maximum generated power was found to be ∼10% greater when copper thermal spreaders were used in comparison to stainless steel thermal spreaders (data not shown). This difference is likely due to the differences in thermal uniformity observed in Fig. 6b. This measured difference in power is less than that depicted in Fig. 2 because hot and cold temperatures are not identical between cases due to unintentional differences in insulation, silver paste, and lack of temperature control as fuel flow rate varies. These differences prevent a more quantitative experimental demonstration of the predictions depicted in Fig. 2.

3.3. Effect of heat removal from the cold side

The data in Fig. 7 were obtained by heat being removed from the thermoelectric (from the cold side) via primarily free convection. In order to enhance heat transfer from this surface using forced convection, a small cooling fan was installed directly above the copper heat sink. Fig. 8a shows the temperatures on each side of the thermoelectric (measured using the integrated thermocouples) and the corresponding temperature differential as a function of the power supplied to the fan, for H_2/air combustion. Note that both hot and cold side temperatures decrease as a function of the power supplied to the cooling fan. However, as fan power increases there is a net increase in temperature differential across the thermoelectric module. Also note that these results were measured using a flow rate of 1.4 SLPM. For the no fan case (Fig. 7), this flow rate resulted in temperatures that were too high for sustained thermoelectric operation. In contrast, with the integrated cooling fan, heat is more efficiently removed from the system, so temperatures are kept below 300 °C even at 1.4 SLPM.

Fig. 8b shows the corresponding electrical power generated and the net power (power generated minus fan power) on the load as a function of fan power. The generated power increases with fan power, eventually reaching a plateau at the highest fan powers. The net power, on the other hand, decreases and eventually the system does not generate net power. Since the flow rates and corresponding powers with and without fan were different, the effect of adding a fan on power cannot be understood unambiguously. However, these results clearly demonstrate that measurable improvements in power generation can be realized through improved cooling. For particular applications where such forced convective cooling is inherently available, such as a flying unmanned air vehicle, these increases in device power

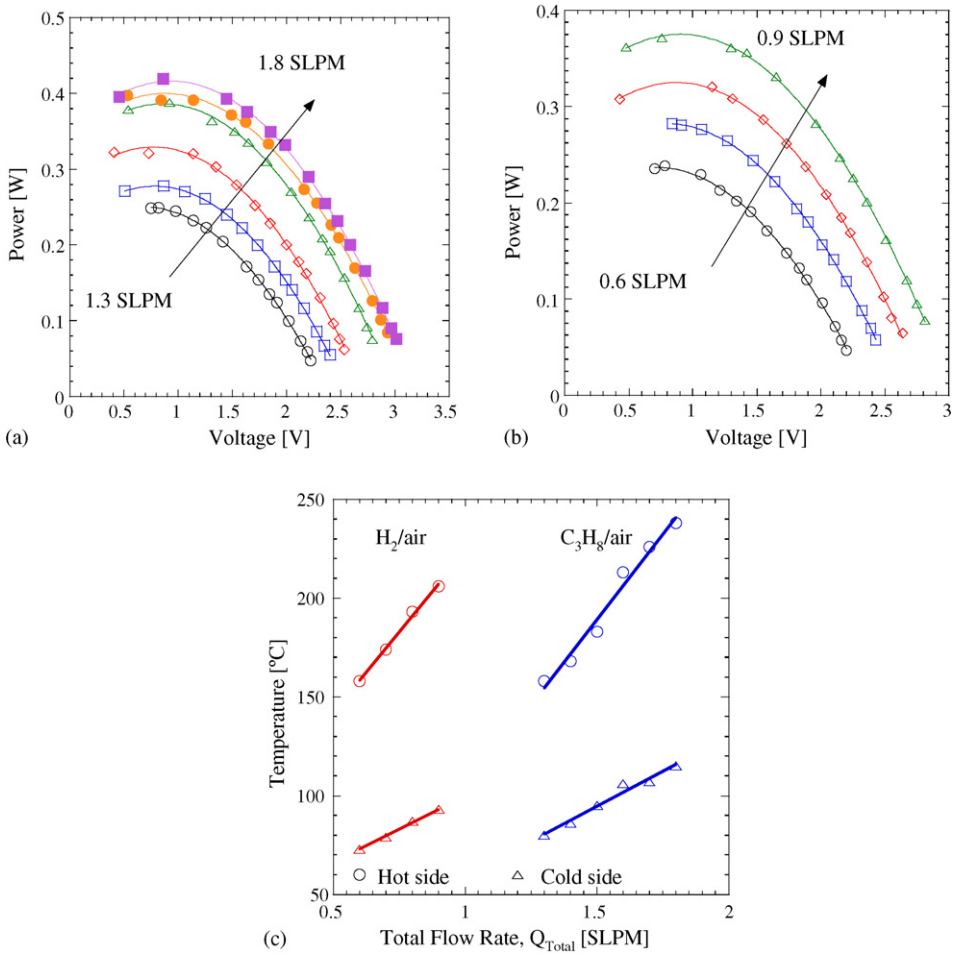

Fig. 7. Thermoelectric power generated vs. voltage for variable total flow rate of both (a) propane and (b) hydrogen in air at stoichiometric conditions. The increase in released thermal energy with increasing flow results in higher temperature differentials across the thermoelectric module, thus increasing the generated power. The flow rate for each curve changes between nearby curves by 0.1 SLPM. The solid lines connect the points, (c) Temperature of hot (triangles) and cold sides (circles) at the maximum power of panels a and b. The lines are linear fits of the experimental points.

can be achieved without requiring a parasitic cooling source, such as the electric fan. Our experiments also point to another challenge, namely that in engineering the temperature difference across a thermoelectric element for maximizing efficiency, it may be difficult to fully decouple the hot and cold sides.

In addition to these simple power generation experiments, using an integrated system with a fan we have been able to successfully run a portable electronic device (a Gameboy® Advance, manufactured by Nintendo) using both hydrogen/air and propane/air combustion for an extended period of time [19]. In other experiments, the overall system power has been increased by using two thermoelectrics simultaneously, with each thermoelectric attached to opposite faces of the microcombustor [19].

3.4. Analysis and discussion on chemical and thermal efficiency of the integrated device

The overall efficiency of converting the chemical energy to electricity has important implications for the practicality of such devices. Fig. 9 displays the conversion and thermal efficiency of the system using a stoichiometric H_2/air mixture. The conversion of the microcombustor is nearly 100%, indicating that the microcombustor is extremely efficient at completely reacting the hydrogen fuel source and releasing its enthalpy.

In order to understand the efficiency of the device, the fraction of enthalpy lost can be determined from

$$\mu_{\text{lost}} = \frac{\hat{H}(x_{\text{in}}, T_{\text{in}}) - \hat{H}(x_{\text{out}}, T_{\text{out}})}{\hat{H}(x_{\text{in}}, T_{\text{in}}) - \hat{H}(x_{\text{out}}, T_{\text{amb}})} \tag{5}$$

where $\hat{H}$ is the enthalpy per unit mass (J g^{-1}) calculated using Chemkin [20], x is mass fraction, T is temperature (K), and the subscripts in, out, and amb correspond to inlet, outlet, and ambient conditions, respectively. The numerator represents the amount of heat released per gram to the microcombustor and the denominator the total amount of energy released. The inlet mass fractions are obtained from the calibrated mass flow controllers, whereas the outlet composition is measured using the gas chromatograph. The inlet and ambient temperatures were both assumed to be 25 °C and the outlet gas temperature was estimated by assuming it to be equal to the measured wall tem-

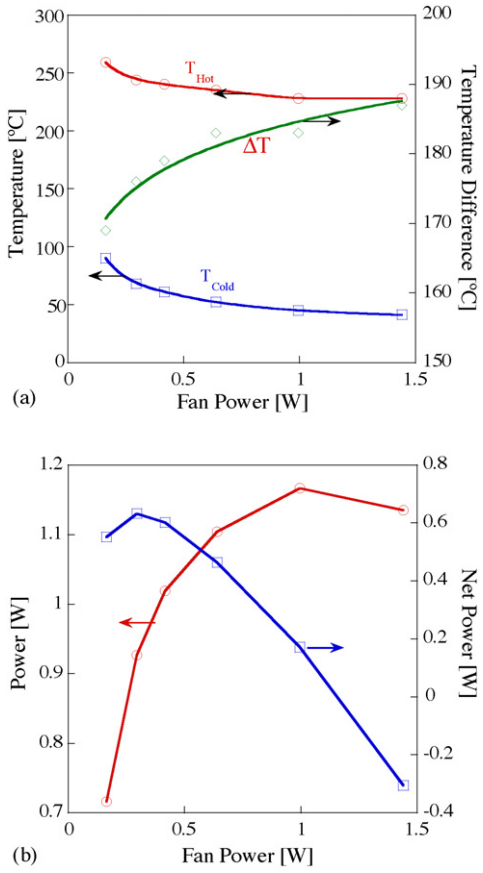

Fig. 8. (a) Hot and cold side temperatures (left vertical axis) and temperature difference (hot minus cold; right vertical axis) as a function of power supplied to cooling fan. As heat transfer from the cold side increases, the net temperature differential also increases. The solid lines just connect the points, (b) Power generated and net generated power vs. fan power. The solid lines connect the points. A stoichiometric H_2/air mixture was fed to the system at a total flow rate of 1.4 SLPM.

perature directly above the reactor outlet. This assumption is reasonable given the small gap height of the combustion chamber. This assumption has been confirmed independently using CFD simulations [18].

In the following discussion, the case of 1.4 SLPM total flow rate is considered. In order to calculate $\hat{H}(x_{out}, T_{amb})$, the steam

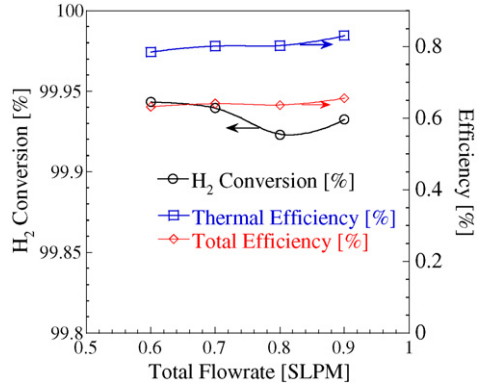

Fig. 9. Thermal and total efficiencies and conversion vs. total volumetric flow rate for a stoichiometric H_2/air mixture. The solid lines connect the points.

leaving the reactor was taken to be condensed, resulting in a total enthalpy generation rate of 88 W. The fractional enthalpy lost was found to be approximately 78%. This calculation indicates that 22% of the chemical power generated, or ~19 W, leaves the system through the outlet gas stream. In order to estimate convective heat losses from the insulated surfaces, an overall heat transfer coefficient of 50 W m^{-2} K^{-1} was assumed based on previous work [18]. Furthermore, an average insulation outer surface temperature was measured using the ThermaCAM Researcher software and found to be approximately 84 °C. With these values and an estimated insulation surface area of 175 cm^2, the estimated power lost through convection on the outside of the insulation is 52 W. The remaining power of ~17 W then passes through the thermoelectric, with an additional $P_{load} = 0.45$ W of power removed as electrical energy, resulting in a thermoelectric efficiency of ~3% (which is comparable to the reported value of 4.5%). This analysis shows that a large fraction of the generated enthalpy is lost through the insulation, indicating that further work is needed to improve packaging and thermal management in our device.

The overall thermal efficiency of the device is defined as the power generated at the load, P_{load}, divided by the chemical energy per unit time fed to the reactor

$$\text{Efficiency}_{\text{Thermal}} = \frac{P_{load}}{(\hat{H}(x_{in}, T_{in}) - \hat{H}(x_{out}, T_{out}))\dot{m}_{total}}, \quad (6)$$

where $\dot{m}_{total}$ is the total mass flow rate (g s^{-1}). The total efficiency accounts also for the energy of the exit stream that could had been used

$$\text{Efficiency}_{\text{Total}} = \frac{P_{load}}{(\hat{H}(x_{in}, T_{in}) - \hat{H}(x_{out}, T_{amb}))\dot{m}_{total}}. \quad (7)$$

Fig. 9 shows that our coupled microcombustor-thermoelectric device converts up to ~0.83% of the chemical power into electrical power based on the thermal efficiency. Using the total amount of heat released, the overall efficiency of the device is ~0.66%. Part of this low efficiency is due to the thermoelectric element but the majority of energy loss is due to inefficient insulation. The hot gases exiting the reactor could be used for other purposes, such as heating a steam reformer or preheating the inlet stream, to allow for a greater range of operation conditions.

In order to put things in perspective, comparison to literature data is useful. A microfabricated power generator has been recently shown to convert radiative heat into electricity using thermal photovoltaic cells, generating 1.02 W at a total efficiency of 2.4% [21]. Thermoionic power generation has been demonstrated to produce 1 μW at an efficiency of 10^{-6}% [22]. Thermal signatures of these systems (critical in military applications) are, based on operating temperatures (600–1000 °C), high. A preliminary thermoelectric micropower generation systems by Schaevitz et al. [10] was capable of producing 0.075 W at a thermal efficiency of 0.02%. This system was not self-igniting with hydrogen and could only produce power with ammonia and butane using pure oxygen but not air. The thermal efficiency running on fuels was not reported. Recently, Yoshida et al. [23] has shown that an integrated thermoelectric system can operate at

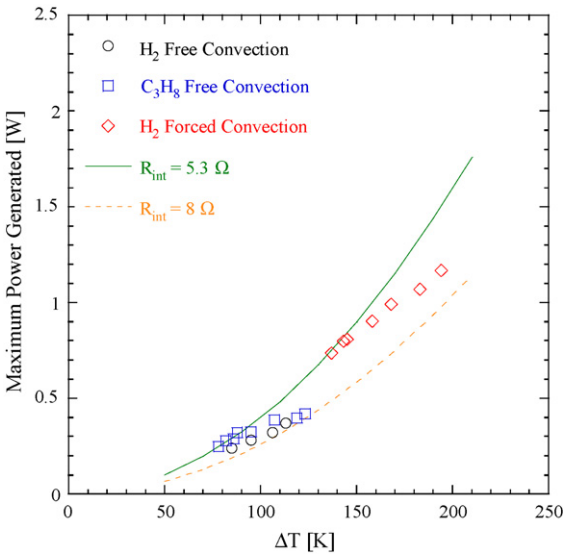

Fig. 10. Comparison of predicted (solid line) and observed (points) power generated using both hydrogen and propane in free and forced convection systems.

higher efficiencies than reported in this work. Two thermoelectric modules were installed on both sides of a smaller microcombustor, capable of generating a smaller power of 0.184 W at a total efficiency of 2.4% using heterogeneous hydrogen combustion over a Pt catalyst. In their integrated device, resistive heaters are required for ignition of the fuel and only combustion of hydrogen could be sustained but not of hydrocarbons.

Fig. 10 shows the maximum power generated, for all flow, fuel type, and forced convection conditions, as a function of temperature differential between the hot and cold sides. Also shown on the graph are two theoretical device performance curves, using Eq. (4) and a Seebeck coefficient of $\Delta S = 0.0288\ \mathrm{V\,K^{-1}}$ (measured using a hot plate with 100 lbs weight and a voltmeter). The solid line uses an internal resistance value of $R_{\mathrm{int}} = 5.3\ \Omega$ (measured using a multimeter at room temperature). Because the internal resistance of the module increases with temperature, the dashed line predicts the performance data using a typical value of $R_{\mathrm{int}} = 8.0\ \Omega$ characteristic of higher temperatures (about 230 °C) [24]. The quadratic relationship between the maximum power generated and the temperature difference is apparent. The acquired data falls between the two predicted power curves, as expected. This suggests that the internal resistance of the module does not increase above 8 Ω at our experimental temperatures.

4. Conclusions

Coupled catalytic microcombustor-thermoelectric devices were fabricated that allow for the conversion of different hydrocarbon fuels into usable electric power. Thermally conductive metal spreaders were used to create a nearly isothermal interface between the microcombustor and the thermoelectric device, which allows for improved power generation. Power generation increases with fuel/air flow rate, with optimal power generation when the load resistance is matched with the internal resistance of the thermoelectric. Power generation was also substantially improved by using forced convection to augment heat removal from the thermoelectric.

An overall thermal efficiency of converting chemical energy to electricity of ~0.8% was measured with a thermoelectric efficiency of ~3%. Efficiency is primarily limited by heat losses through the insulated walls, indicating that even higher system efficiencies are possible through improved thermal management. The large disparity in reported thermal efficiencies between various works reported in the recent literature and this work demonstrate the importance of understanding key factors controlling the performance of integrated combustor-thermoelectric devices. This work has provided insights into this issue and highlighted the importance for improved system designs that will be the subject of future work.

Acknowledgments

This work has been funded through the Army Research Laboratory Composite Materials Research program at the University of Delaware Center for Composite Materials. The assistance of John McCormick and Justin Clews with the TEM and the IR, respectively, is greatly appreciated.

Appendix A. Effect of compressive force on power generation

The thermal contact between the elements of the integrated device plays an important role on the observed Seebeck coefficients and ultimately on the power generation. The thermal expansion coefficient of the thermoelectric module used is quite large ($2 \times 10^{-6}\ ^{\circ}\mathrm{C}^{-1}$). As a result, a compressive loading is required. A set of experiments was performed in order to study the effect of compressive force on the performance of the device. A calibrated 4 in. spring from Larson Systems Inc. with a maximum capacity of 250 lbs was placed directly above the heat sink and the displacement was adjusted by tightening the C-clamp. For safety reasons, the spring was harnessed in two machined end pieces with abraded edges to prevent slippage.

Various loadings were used in this study (approximately 30, 73, 115, and 158 lbs). The system consisted of a stoichiometric H_2/air mixture and only free convection was used to cool the cold side of the thermoelectric module. The results are depicted in Fig. A1. The open circuit voltage data exhibit a linear dependence on ΔT (Fig. A1a), validating the assumption that Seebeck coefficients are weak functions of temperature. Using linear regression, one can estimate the ΔS value (see Eq. (2)) from the slope. The increase in apparent ΔS was substantial after increasing the loading from 73 to 115 lbs, as seen in Fig. A1a. By overlaying the measured ΔS value of $0.0288\ \mathrm{V\,K^{-1}}$ (dashed line, termed hot plate) from the hot plate experiment (used in Fig. 10), the data of this paper lies close to the 73 lbs experimental set, indicating the approximate compressive load using the C-clamp for the data reported in this paper.

The observed maximum powers generated for closed circuit with the potentiometer are plotted in Fig. A1b. It is clear that higher compressive loading increases both the maximum power generated as well as the efficiency of the integrated device.

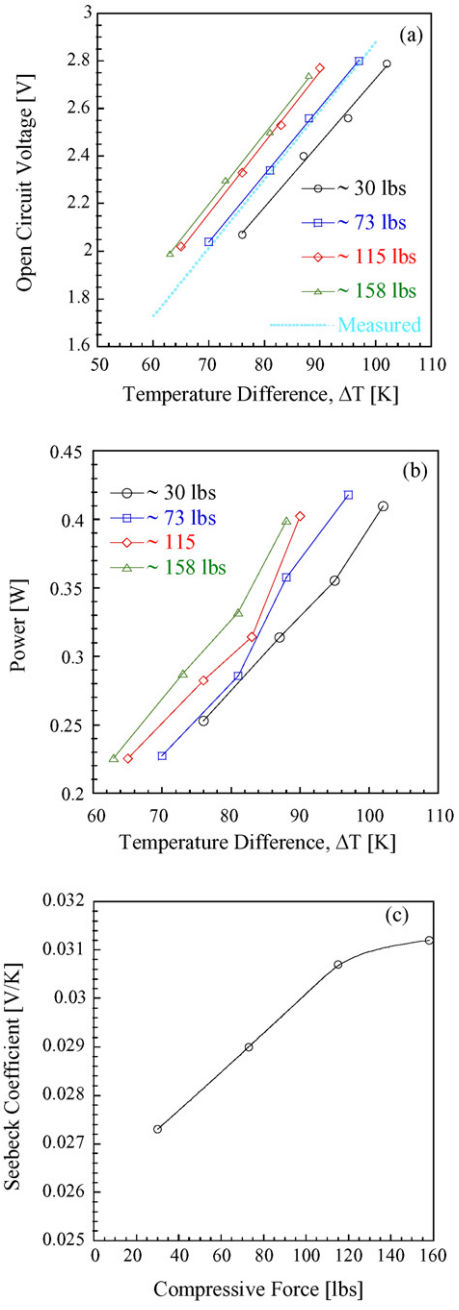

Fig. A1. (a) Open circuit voltage vs. temperature differential for varying compressive loadings, (b) maximum power generated vs. temperature differential at the same conditions, (c) estimated ΔS value vs. applied force using linear regression in panel a. The system conditions are the same as those in Fig. 7b, namely a stoichiometric H_2/air mixture under free convection.

Fig. A1c shows the estimated ΔS values as a function of the compressive force. As the force increases, the ΔS value also increases, which is consistent with the hypothesis that the difference of thermal expansion coefficients of the thermoelectric contacts and the frame causes a loss of thermal contact at higher temperatures. The value of ΔS appears to reach an asymptotic limit at higher forces. Assuming that the temperature differential remained constant, the thermal efficiency of the device would increase by 17% (resulting in a higher efficiency of 0.97%) if an approximate compressive loading of 158 lbs was applied.

References

[1] L. Sitzki, K. Borer, E. Schuster, P.D. Ronney, S. Wussow, Proceedings of The Third Asia-Pacific Conference on Combustion, Seoul, Korea, 2001.
[2] A.S. Patil, T.G. Dubois, N. Sifer, E. Bostic, K. Gardner, M. Quah, C. Bolton, J. Power Sources 136 (2004) 220–225.
[3] J. Ahn, P.D. Ronney, Proceedings of Fourth Joint Meeting U.S. Sect. Comb. Inst., Philadelphia, PA, 2005.
[4] C.M. Miesse, R.I. Masel, M. Short, M.A. Shannon, Comb. Sci. Tech. 9 (2004) 77–92.
[5] C. Jensen, R.I. Masel, G.V. Moore, M. Shannon, AIChE J. 50 (2004) 3206–3214.
[6] L.R. Arana, S.B. Schaevitz, A.J. Franz, K.F. Jensen, M.A. Schmidt, J. MEMS 12 (2003) 600.
[7] A. Cohen, P.D. Ronney, U. Frodis, L. Sitzki, E. Meiburg, S. Wussow, Microcombustor and combustion-based thermoelectric microgenerator U.S. Patent No. 6,613,972 (2003).
[8] D.G. Norton, D.G. Vlachos, Proceedings of the Combustion Institute 30 (2005) 2773–2480.
[9] D.G. Norton, E.D. Wetzel, D.G. Vlachos, Ind. Eng. Chem. Res. 43 (2004) 4833–4840.
[10] S.B. Schaevitz, A.J. Franz, K.F. Jensen, M.A. Schmidt, Proceedings of The 11th International Conference on Solid-State Sensors and Actuators, Munich, Germany, 2001.
[11] K. Yoshida, K. Kobayashi, T. Nakajima, D. Satoh, S. Tanaka, M. Esashi, Proceedings of Internaional Workshop on Power MEMS, Tsukuba, Japan, 2002, pp. 98–101.
[12] D.G. Norton, D.G. Vlachos, Chem. Eng. Sci. 58 (2003) 4871–4882.
[13] D.G. Norton, D.G. Vlachos, Comb. Flame 138 (2004) 97–107.
[14] S.R. Deshmukh, D.G. Vlachos, Ind. Eng. Chem. Res. 44 (2005) 4982–4992.
[15] S.R. Deshmukh, D.G. Vlachos, Chem. Eng. Sci. 60 (2005) 5718–5728.
[16] D.J. Quiram, I.M. Hsing, A.J. Franz, K.F. Jensen, M.A. Schmidt, Chem. Eng. Sci. 55 (2000) 3065–3075.
[17] A. Usai, S. Silvestrini, Revue De Metallur.-Cahiers D Informat. Techn. 95 (1998) 786–788.
[18] D.G. Norton, E.D. Wetzel, D.G. Vlachos, Ind. Eng. Chem. Res. 45 (2006) 76–84.
[19] D.G. Norton, K.W. Voit, T. Brüggemann, E.D. Wetzel, D.G. Vlachos, Proceedings of The 24th Army Science Conference, Orlando, FL, 2004.
[20] R.J. Kee, F.M. Rupley, J.A. Miller, Chemkin-II: A FORTRAN chemical kinetics package for the analysis of gas phase chemical kinetics. Sandia National Laboratories Report, SAND89-8009. Livermore, CA, 1991.
[21] W.M. Yang, S.K. Chou, C. Shu, Z.W. Li, Appl. Phys. Lett. 84 (2005) 3864–3866.
[22] C. Zhang, N. Najafi, L.P. Bernal, P.D. Washabaugh, Proceedings of 12th International Conference on Solid-state Sensors, Actuators and Microsystems, Boston, MA, USA, 2003, pp. 40–44.
[23] K. Yoshida, S. Tanaka, S. Tomonari, D. Satoh, M. Esashi, J. Microelectromech. Syst. 15 (2006) 195–203.
[24] J. Bass, Personal communication (2006).